

See discussions, stats, and author profiles for this publication at: <https://www.researchgate.net/publication/231697246>

# Brownian Dynamics Modeling of Flow-Induced Birefringence and Chain Scission in Dilute Polymer Solutions in a Planar Cross-Slot Flow

ARTICLE *in* MACROMOLECULES · JANUARY 2005

Impact Factor: 5.8 · DOI: 10.1021/ma0491255

---

CITATIONS

17

---

READS

21

3 AUTHORS, INCLUDING:



Chih-Chen Hsieh

National Taiwan University

32 PUBLICATIONS 667 CITATIONS

SEE PROFILE

# Brownian Dynamics Modeling of Flow-Induced Birefringence and Chain Scission in Dilute Polymer Solutions in a Planar Cross-Slot Flow

Chih-Chen Hsieh, Seung Joon Park, and Ronald G. Larson\*

Department of Chemical Engineering, University of Michigan, Ann Arbor, Michigan 48109

Received May 4, 2004; Revised Manuscript Received November 12, 2004

**ABSTRACT:** Bead–spring Brownian dynamics simulations are herein used to model flow-induced chain scission in dilute polymer solutions in a planar cross-slot flow. The flow field is obtained by finite-element simulation for a Newtonian fluid at low Reynolds number ( $Re = 4.5$ ), with the flow assumed to be unaffected by the polymer. Chain scission is defined to occur when any spring bears a force over a preset critical spring force. Multiple scission of the same chain in a single pass through the device is allowed. In the simulations, we observed both chain halving and quartering as reported in the experimental literature. However, in contrast to the common view that breakage occurs only in the stagnation point region, we find that the strong shearing flow generated near the walls of the inlet channel prestretches polymer molecules considerably, leading to breakage near the corner where an extensional flow is present. We also predict flow birefringence, which supports our finding that shear plays a significant role in chain scission in this geometry.

## I. Introduction

When a polymer molecule is subjected to a strong elongational flow, it deviates from its equilibrium state, experiences a coil–stretch transition, and finally reaches a highly extended state. If the elongational flow is very strong and the polymer molecule cannot sustain the tension imposed by the flow, it eventually breaks into smaller pieces. Flow-induced polymer degradation is very common, but is usually not desired. High-molecular-weight polymers are often used as viscosifiers and as drag-reducing agents in turbulent flows<sup>1</sup> where degradation reduces their effectiveness and thus one seeks to avoid it. Flow-induced polymer degradation also occurs in gel permeation chromatography (GPC) and results in inaccurate measurements of the molecular weight distribution. On the other hand, polymer chain scission can convert a highly polydisperse polymer sample into a more monodisperse one.<sup>2,3</sup> Thus, to either minimize or optimize the degree of degradation, a thorough understanding of flow-induced polymer chain scission is essential.

Many experimental and theoretical studies have been carried out to investigate the mechanism of polymer mechanical degradation over the past 20 years. Yu et al. investigated polymer degradation using a high-shear concentric cylinder viscometer and reported that the molecular weight distribution narrowed after chain scission.<sup>2</sup> They also concluded that the chains broke preferentially at their centers. Keller and co-workers<sup>4,5</sup> found that when a dilute polystyrene solution was pumped into a cross-slot device, a bright birefringent line emerged along the center axis of the exit plane once the elongational rate exceeded a certain limit. By observing this sudden jump in the magnitude of the flow birefringence, they were able to identify the relaxation time and molecular weight distribution of a polymer mixture. By applying the same technique, Odell et al.<sup>6</sup> measured chain scission in dilute polystyrene solutions in the cross-slot device. Two important results were

reported: (1) a highly localized birefringent line along the exit axis was observed and (2) polystyrene molecules of  $M_w = 2 \times 10^7$  in Decalin were found to be broken roughly in the middle three successive times, reducing their molecular weight to roughly one-eighth the original value after multiple passes through the device at a fixed strain rate of  $6 \times 10^4 \text{ s}^{-1}$ . The results of flow birefringence and chain scission measurements, including the observed midpoint scission, suggested that the strong elongational flow generated at the center of the cross-slot was the cause of the chain scission and that the polymer chains were fully stretched before breaking.

The studies of Merrill and Horn<sup>7,8</sup> of a dilute polystyrene solution passing through a sudden contraction in a turbulent flow also demonstrated the occurrence of the midpoint scission. Keller and Odell<sup>9,10</sup> further determined that the critical elongation rate ( $\dot{\epsilon}_f$ ) at the onset of chain scission is inversely proportional to the square of the molecular weight of the polymer chain ( $M_w$ ) in a cross-slot device. However, Nguyen and Kausch<sup>11,12</sup> observed a different scaling law,  $\dot{\epsilon}_f \propto M_w^{-1}$ , when investigating the degradation of a dilute polystyrene solution passing through a contraction. In their experiments, a variation of the contraction angle from  $180^\circ$  (sudden contraction) to  $5^\circ$  seemed to have no significant influence on the observed scaling law. There are, however, two essential differences between the experiments of Keller and co-workers and those of Nguyen and Kausch. First, the cross-slot device used by the former group possesses a stagnation point, while the contraction flow used by Nguyen and Kausch does not. Second, most of the work of Keller et al. was carried out at a Reynolds number  $Re < 1000$  while  $Re > 1000$  in Nguyen and Kausch's experiments.<sup>13</sup> These two differences are considered to be possible causes for the different scaling laws observed.

While the scaling law  $\dot{\epsilon}_f \propto M_w^{-2}$  can be explained by simple viscous drag forces on a fully extended chain in laminar flow,<sup>10,14</sup> the cause of the scaling law  $\dot{\epsilon}_f \propto M_w^{-1}$  is not well understood. Rabin<sup>15</sup> proposed an explanation for this discrepancy using the “yo-yo” model<sup>16</sup> which assumed that the polymer chain unravels like a “yo-

\* Corresponding author. Telephone: 734-936-0772. Fax: 734-763-0459. E-mail: rlarson@engin.umich.edu.

yo-yo" with a stretched center part and two coiled ends in an elongational flow. Rabin argued that in a very strong transient elongational flow such as a contraction flow the chains do not have enough time to unravel fully before they break. Thus, the critical elongation rate for chain scission is inversely proportional to the square of the dimension of the stretched center segment of the polymer which is comparable to its equilibrium coil size. As a result, a scaling law of  $\dot{\epsilon}_f \propto M_w^{-2\nu}$  ( $\nu$  is the Flory exponent = 0.5–0.6) was predicted. This scaling law is very similar to that observed by Nguyen and co-workers in the converging flow. However, Smith et al.<sup>17</sup> and Larson et al.<sup>18</sup> have shown that in a very strong steady elongational flow (Deborah number  $\sim 55$ ), the "yo-yo" or "dumbbell" mode of unraveling only occurs for 15% of the molecules in the flow.

Despite the above divergences between the experiments of Odell and co-workers and those of Nguyen and Kausch, both experiments showed that chain scission takes place at the center of a chain and also showed that a chain breaks sequentially into halves, quarters, and then eighths if the imposed elongation rate is much higher than the critical elongation rate for the scission of the original unbroken chains.

Reese and Zimm<sup>19</sup> used flow through a sudden contraction to fracture T7 DNA molecules in a dilute solution. The resultant distribution of the fragments of both single and double-stranded DNA after degradation also suggested the predominance of midpoint scission, but gave a broader fragment distribution than that reported in the previous studies using polystyrene and PEO. Atkins and Taylor<sup>20</sup> used an opposed-jet device to degrade  $\lambda$ -phage DNA and used electrophoresis to detect the molecular weight distribution of DNA fragments after the degradation. Once again, chain halving and quartering were demonstrated.

Buchholz et al.<sup>3</sup> pumped semidilute solutions of three different water-soluble, highly dispersed, high-molecular-weight polymers through a capillary entrance region and analyzed the evolution of the polymer molecular weight distribution after each pass through the capillary. The experimental results were fit with a statistical model, the best fitting parameters were extracted, and three conclusions were drawn. First, for the flow studied, on average a chain experiences more than one scission event during a single pass. Second, chain scission occurs predominantly in the central 20% of the chain, i.e., near the chain's midpoint. Third, this chain degradation process effectively reduces the polydispersity of the initially highly polydispersed polymer samples.

Very recently, Islam et al.<sup>13</sup> performed chain-scission experiments on an aqueous PEO solution in a cross-slot device similar to Odell and co-workers' design, and for the first time observed both scaling laws  $\dot{\epsilon}_f \propto M_w^{-2}$ , and  $\dot{\epsilon}_f \propto M_w^{-1}$  found by Odell and co-workers, and by Nguyen and Kausch, respectively. By comparing their data with those obtained from the early studies, Islam et al. suggested that the different scaling laws are caused by the presence or absence of an inertial effect and are not due to the presence or absence of a flow stagnation point. Although the two different scaling laws were observed in their study, midpoint scission was not confirmed, due to the use of a polydisperse polymer.

In summary, we find a lack of consistency among different studies over the past 20 years. Since it is very difficult to exclude all unwanted flow modifications from these flow devices, such as those due to the entry

contraction (valve), some inevitable asymmetry in the flow cell, instabilities or secondary flows induced by bounding walls on the top and bottom of the device,<sup>21</sup> or turbulent flow, most experimental chain scission results are probably influenced by several effects beyond simple extensional, laminar, flow. We hope the simulation results reported here can shed some light on these experimental results and motivate additional, careful, experiments.

While there has been a long history of experimental and theoretical studies of the flow behavior of dilute polymer solutions, a more accurate simulation procedure, namely Brownian dynamics simulations, has only become computationally affordable within the past decade. Brownian dynamics (BD) simulations have been shown capable of predicting accurately polymer conformations and conformational transitions in time-dependent shear and elongational flows, as well as the macroscopic stresses of dilute polymer solutions.<sup>22–24</sup> Consequently, BD simulations can now serve as a tool to help us explore polymer behavior in a dilute solution. There have been several studies using BD simulations to simulate chain scission in a uniform elongational flow and in converging flows.<sup>19,25–30</sup> The pioneering work is that of Reese and Zimm<sup>19</sup> who used BD simulations with a bead-spring model to predict the distribution of the fragments of DNA after scission in a converging flow. The effect of HI was neglected, and a critical spring length was chosen to be the criteria for chain scission. The predicted fragment distribution of DNA was very uniform and was broader than the experimental results. de la Torre and co-workers also investigated polymer chain scission extensively using BD simulations in both a steady uniaxial extensional flow<sup>25,26</sup> and a converging flow.<sup>27–30</sup> The flow fields used in their studies were simplified, and the simulations were only carried out for the molecules flowing along the centerline of the converging flows. Because of the use of the simplified flow field, the detailed flow field throughout a flow device cannot be accurately captured in the simulations. In a steady uniaxial extensional flow, they found that the chain fragment distribution varies from sharply peaked (midpoint scission) to uniform (random scission), depending on the flow strength.<sup>26</sup>

de la Torre and co-workers also investigated the molecular weight dependence of the critical strain rate and found that hydrodynamic interaction (HI) has a significant influence on the predicted scaling law in a converging flow. In a steady extensional flow, on the other hand, the predicted scaling of  $\dot{\epsilon}_f \propto M_w^{-2}$  is in agreement with the experimental observations and is independent of the presence or the absence of HI. The fact that hydrodynamic interaction has little or no effect on the predicted scaling law  $\dot{\epsilon}_f \propto M_w^{-2}$  in simple extensional flow is anticipated because under this flow a chain is likely to unravel fully before breaking. Since HI is very weak for a chain at its extended configuration, including HI in the simulations is not likely to change the earlier scaling law predicted without HI. However, in converging flow  $\dot{\epsilon}_f \propto M_w^{-2}$  was predicted without HI while  $\dot{\epsilon}_f \propto M_w^{-1}$  was predicted with HI. Although the latter scaling law coincides with that reported by Nguyen and Kausch, a recent study of Islam et al.<sup>13</sup> suggested that the inertial effect is the cause of this change.

While HI must be accurately included if one wants to predict quantitatively the chain scission process,<sup>24,31</sup>

it is currently not feasible to do so, because of the huge demand on computer power and the imperfection of the current methods for including HI in BD simulations. Nevertheless, since most molecules break only when they are nearly fully extended, the presence or absence of explicit HI in the simulations will mainly affect the critical tension at which the extended chains break. But since we take this as an adjustable parameter, we do not believe the absence of HI in our simulations will affect qualitatively our predictions *at a fixed molecular weight*. If the molecular weight is changed, the critical tension will presumably need to be altered, however, if we are to match simulation results to experiments at multiple molecular weights. As will be discussed later, predicting *a priori* the scaling law of critical strain rate vs the molecular weight of polymer chain is beyond the scope of the present study because of our method of determining the drag coefficient in the absence of explicit HI. Please see the Appendix for a more detailed discussion on the issue of HI.

In this study, we use a nonlinear, finitely extensible-spring law and a reasonable critical spring force, combined with an accurate flow field computed by a finite-element method, in our BD simulations. We also allow each chain to break as many times as the specified criterion for scission is reached in a single pass through the device. In earlier studies, simulations were only performed for the polymer chains flowing along the center line of the device, where there is a strong elongational flow, and no shear. However, motivated by the BD simulations that revealed an effect of preshearing on the unraveling of a polymer chain in the subsequent elongational flow,<sup>32</sup> we performed our simulations over the whole device.

This paper is organized as follows. In section II, we describe the finite element method used to generate the flow field in the cross-slot device and briefly review the Brownian dynamics simulation technique. The method of estimating parameter values and details of the simulations are also described. In section III, the simulated flow birefringence produced in the cross-slot is presented, and compared with experimental observations. We also present molecular weight distribution of chain fragments after scission, the locations in the flow field where the chains break, and the causes of chain breakage. In section IV, we give the conclusions.

## II. Simulation Method

**The Model System.** This study mimics the work of Odell and Keller<sup>10</sup> in which aqueous solutions of monodisperse poly(ethylene oxide) (PEO) with molecular weight  $M_w = 1.4 \times 10^6$  were pumped into a cross-slot device and experienced chain scission. The width of the cross-slot is 300  $\mu\text{m}$ , and the depth is 1.6 mm. In our simulations, we take the initial polymer to be monodisperse in molecular weight and take the width and the length of the slot channels to be 300  $\mu\text{m}$  while assuming that the depth is much larger than the width so that the flow can be considered to be planar. In the experiments, the Reynolds number  $Re = \rho D v_{\text{Avg}} / \eta_s$  at the flow rate for which the PEO undergoes degradation is 45000 if the viscosity of the PEO solutions is estimated to be that of water, 1 cP, and the density to be 1  $\text{g}/\text{cm}^3$ . However, at  $Re = 45000$  the flow is expected to be turbulent. To keep our model system simple, we therefore choose to lower the Reynolds number to a value corresponding to a laminar flow while keeping the

Deborah number  $De = \tau_1 \dot{\epsilon}$  the same as in the experiments where  $\dot{\epsilon}$  is the extensional rate. If the Deborah number remains unchanged, the polymer in the solution will experience the same magnitude of drag force from the solvent as in the experiments. To achieve this in the simulations, we increase the solvent viscosity 100-fold from 1 cP to 1 poise and make the flow rate 100 times lower. The nominal elongation rate  $\dot{\epsilon}_{\text{nominal}}$  in a cross-slot device can be defined by  $\dot{\epsilon}_{\text{nominal}} = Q/w^2d$  where  $Q$  is the volumetric flow rate, and  $d$  and  $w$  are the depth and width of the cross-slot, respectively. The value of  $\dot{\epsilon}_{\text{nominal}}$  was 500000  $\text{s}^{-1}$  in the experiments of Odell and Keller<sup>10</sup> while we have  $\dot{\epsilon}_{\text{nominal}} = 5000 \text{ s}^{-1}$  in our simulations due to the decrease in the flow rate. Because we increase the viscosity by 100-fold, the longest relaxation time of PEO increases by a factor of 100. As a result, the Deborah number  $De = \tau_1 \dot{\epsilon}_{\text{nominal}}$  remains unaffected, but the Reynolds number  $Re$  is reduced to  $Re = 4.5$ . Chain scission experiments with viscosified solvents are feasible, and would provide a direct experimental test of the predictions made here.

**Finite Element Simulation of the Flow Field in the Cross-Slot Device.** While the presence of polymer in the solution can in general change the flow field in the cross-slot device, in the case of a sufficiently dilute polymer solution, its effect on the flow becomes negligible. Therefore, we assume here that the Newtonian flow field is not disturbed by the viscoelasticity of the polymer molecules. The steady-state isothermal flow of an incompressible Newtonian fluid is governed by the continuity and Navier–Stokes equations as follows:

$$\nabla \cdot \mathbf{v} = 0 \quad (1)$$

$$\rho \mathbf{v} \cdot \nabla \mathbf{v} = -\nabla p + \eta_s \nabla^2 \mathbf{v} \quad (2)$$

where  $\mathbf{v}$  is the velocity vector,  $\rho$  the density,  $p$  the pressure, and  $\eta_s$  the solvent viscosity.

We use a Galerkin finite element method to discretize the above set of governing equations. The velocity and pressure unknowns are approximated by Galerkin basis functions<sup>33</sup>

$$\mathbf{v} = \sum_i \psi_i \mathbf{v}_i, p = \sum_i \phi_i p_i \quad (3)$$

where  $\mathbf{v}_i$  and  $p_i$ , respectively, are the velocity and pressure values, and  $\psi_i$  and  $\phi_i$  the bilinear and biquadratic basis functions at the nodes of the finite elements. The above equations weighted by the basis functions and integrated by parts, result in the following weak forms:

$$\langle \nabla \cdot \mathbf{v}; \phi \rangle = 0 \quad (4)$$

$$\langle \rho \mathbf{v} \cdot \nabla \mathbf{v}; \psi \rangle + \langle -p \mathbf{I} + \eta_s (\nabla \mathbf{v} + \nabla \mathbf{v}^T); \nabla \psi \rangle = \langle \langle -p \mathbf{I} + \eta_s (\nabla \mathbf{v} + \nabla \mathbf{v}^T) \cdot \mathbf{n}; \psi \rangle \rangle \quad (5)$$

where  $\mathbf{I}$  is the unit tensor and  $\mathbf{n}$  is the normal vector along the boundary of the domain. In the above equations, the symbols  $\langle \rangle$  and  $\langle \langle \rangle \rangle$  stand for domain and boundary line integrals, respectively.

The geometry and boundary conditions used in this study are shown in Figure 1. Because of the symmetry of the cross-slot geometry only one-quarter of the whole domain is considered for the simulation. The imposed boundary conditions are as follows:



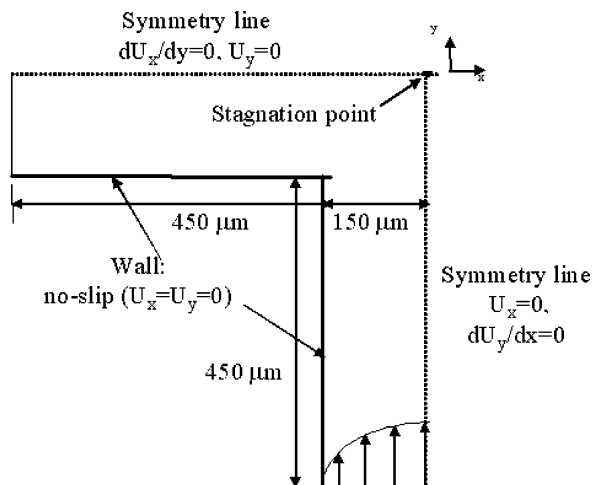


**Figure 1.** Schematic diagram of the cross-slot device and boundary conditions used in the finite element simulations. Because of the symmetry of the cross-slot geometry, only one-quarter of the whole domain is considered for simulation.

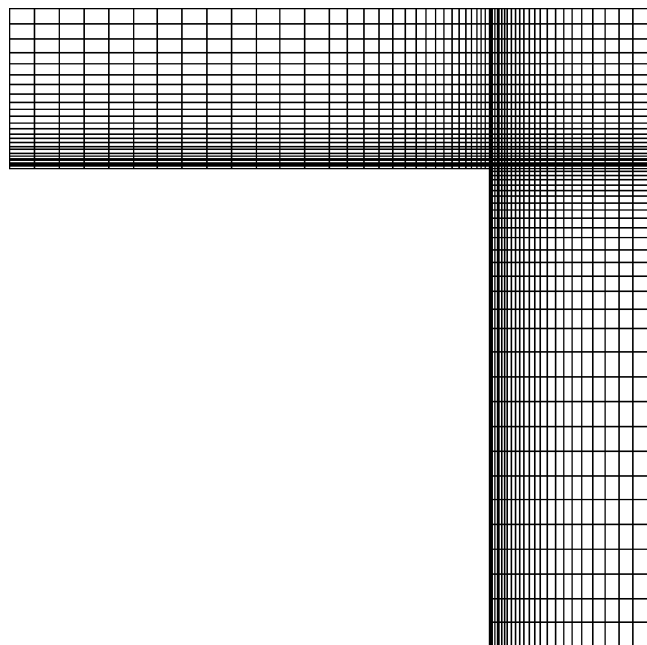


**Figure 2.** Finite element mesh used in this study. A total of 8721 nodes are used.

- (i) Along the inlet boundary, fully developed velocity profile,  $U_x = 0$ ,  $U_y = U_y(x)$ .
- (ii) At the wall, no slip condition,  $U_x = U_y = 0$ .
- (iii) Along the inflow symmetry line,  $U_x = 0$ ,  $dU_y/dx = 0$ .
- (iv) Along the outflow symmetry line,  $dU_x/dy = 0$ ,  $U_y = 0$ .
- (v) Along the outflow boundary,  $dU_x/dx = 0$ ,  $U_y = 0$ .

The finite element mesh used in this study is shown in Figure 2. We use a finer mesh near the wall due to the high velocity gradient there and a total of 8721 nodes are used in this simulation. The finite element simulation is performed at a Reynolds number of  $Re = 4.5$ . Figure 3 shows the predicted flow field in the cross-slot device and indicates the strong extensional flow near the stagnation point. Mirror images were used for generating the flow field over the whole cross-slot device. This flow field will be used in the Brownian dynamics simulations below.

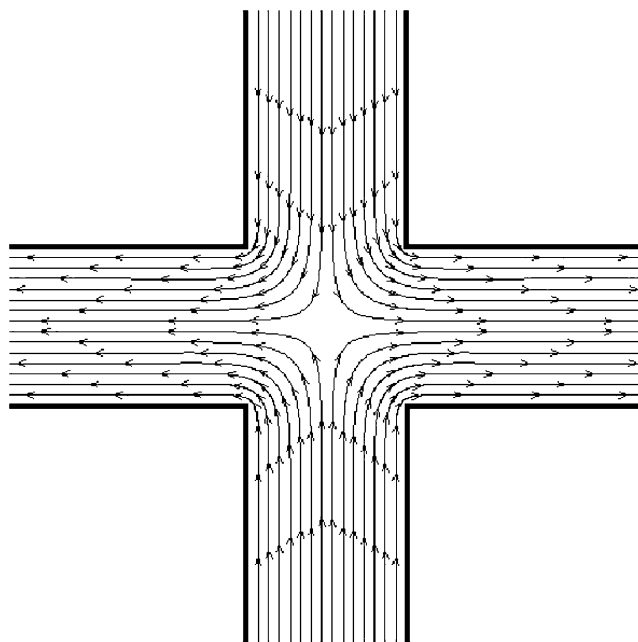


**Figure 3.** Flow field predicted by a finite element simulation in the cross-slot device at  $Re = 4.5$ . Mirror images are used to generate the flow field over the whole domain.

**Bead–Spring Model.** In this study the polymer molecules are simulated by the well-known bead–spring model using Brownian dynamics simulations. We briefly summarize the model below; more details can be found in Li and Larson.<sup>22</sup> Notice that, except for a few runs to be described later, hydrodynamic interaction is not included in the present study. A discussion for the possible consequence of this simplification can be found in the Appendix. The bead–spring model represents the polymer as a string of  $N$  beads connected by  $N - 1$  springs. The flow-induced drag force acts on the beads and the elasticity of the polymer is represented by the springs. The motion of the beads can be obtained by solving the force–balance equation:

$$\tilde{F}_i^{drag} + \tilde{F}_i^{spring,bead} + \tilde{F}_i^{Brownian} = 0 \quad (6)$$

where  $i$  represents the  $i$ th bead, and the three forces are the drag force, the spring force, and the Brownian force, respectively. When hydrodynamic interaction is not considered, the force terms can be expressed as

$$\begin{aligned} \tilde{F}_i^{drag} &= -\zeta(\tilde{r}_i - \tilde{v}_i) \\ \tilde{F}_i^{spring,bead} &= \tilde{F}_i^{spring} - \tilde{F}_{i-1}^{spring} \\ \tilde{F}_i^{Brownian} &= \left( \frac{6k_B T \zeta}{\Delta t} \right)^{1/2} \tilde{n}_i \end{aligned} \quad (7)$$

where  $\tilde{r}_i$  is the coordinate vector of bead  $i$ ,  $\tilde{r}_i$  is the velocity of this bead,  $\tilde{v}_i$  is the velocity of the surrounding fluids,  $\zeta$  is the bead drag coefficient, and  $\tilde{n}_i$  is a random vector uniformly distributed in each of three directions over the interval  $[-1, 1]$ .

The spring force acting on bead  $i$ ,  $\tilde{F}_i^{spring,bead}$ , is the net force from the two springs connected to bead  $i$ . The

spring force in spring  $i$  is represented by the Cohen–Padé approximation to the inverse Langevin function,<sup>34</sup> which is

$$F_i^{spring} = \frac{k_B T}{b_K} \frac{3 - \lambda_i^2}{1 - \lambda_i^2} \quad (8)$$

where  $b_K$  is the Kuhn segment length, and  $\lambda_i$  is the ratio of the spring length to the maximum spring length. The vector  $F_i^{spring}$  is oriented in the same direction as spring  $i$ . The Cohen–Padé approximation is a nonlinear spring force law for which the spring force goes to infinity as  $\lambda_i$  approaches unity. Combining eqs 6–8, and using an explicit integration scheme, we can write the equation of motion for the beads as

$$\tilde{r}_{i,t+\Delta t} = \tilde{r}_{i,t} + \left[ \tilde{v}_i + \frac{F_i^{spring,bead}}{\zeta} + \left( \frac{6k_B T}{\zeta \Delta t} \right)^{1/2} \tilde{n}_i \right] \Delta t \quad (9)$$

To determine the appropriate number of beads and the time step size for this study, we have carried out simulations with 14, 28, and 56 beads with different time steps until the simulation results converged. All the results shown below are from simulations with 28 beads, which give very similar results to those obtained with  $N = 56$  beads. The time step we use is  $\Delta t = 1.4 \times 10^{-10}$  s for all cases, and our results are insensitive to refinements of this time step.

**Bead–Spring Parameters.** Before performing the simulations, we need to determine the parameters from the physical properties of the polymers. From eq 9, we need the contour length of the polymer molecule  $L$ , bead drag coefficient  $\zeta$ , and the Kuhn length  $b_K$  to perform the simulations. For a polymer molecule, the contour length  $L$  can be estimated by

$$L = N_K b_K = 0.82nl \quad (10)$$

where  $N_K$  is the number of Kuhn steps,  $n$  is the number of backbone units in the polymer, and  $l$  is the average length of a backbone unit. The constant 0.82 arises from the tetrahedral bonding angles between the backbone bonds.<sup>35</sup> For PEO,  $n = M_w/14.667$  and  $l = 1.46$  Å. This bond length  $l$  is taken as the average over the single C–C bond ( $l = 1.54$  Å) and two C–O bonds ( $l = 1.43$  Å) in each monomer of the PEO backbone. From Virk,<sup>36</sup> the radius of gyration of a monodisperse polymer can be obtained from

$$R_G^3 = M[\eta]_0/A \quad (11)$$

where  $M$  is the molecular weight of polymer and  $[\eta]_0$  is the intrinsic viscosity. The constant  $A$  is  $3.1 \times 10^{24}$  and is defined by  $(0.8)6^{3/2}\Phi$  with Fox–Flory parameter  $\Phi = 2.66 \times 10^{23}$ , where the factor of 0.8 accounts for the use of the good solvent.<sup>36</sup> The intrinsic viscosity can be calculated from the formula

$$[\eta]_0 = \kappa M^a \quad (12)$$

where  $\kappa$  is the Mark–Houwink coefficient, and  $a$  is the exponent. In a  $\Theta$  solvent,  $a$  is 0.5, becoming larger in a good solvent. For PEO in water containing 0.1 M NaNO<sub>3</sub> with 1.0 wt % 2-propanol and 200 ppm hydrazine to prevent oxidation and microbial degradation,  $k = 0.17$  cm<sup>3</sup>/gm, and  $a = 0.57$ .<sup>13</sup> Substituting eq 12 into eq 11,

the average end-to-end square distance  $\langle R^2 \rangle_0$  can be related to the molecular weight and the intrinsic viscosity by

$$N_K b_K^2 = \langle R^2 \rangle_0 = 6R_G^2 = 6 \left[ \frac{M[\eta]_0}{A} \right]^{2/3} \quad (13)$$

Combining eq 13 and 10, we get  $N_K$  and  $b_K$  as

$$b_K = \frac{\langle R^2 \rangle_0}{L} = 7.317 \frac{(\kappa M^{1+a} A^{-1})^{2/3}}{nl} \quad (14)$$

$$N_K = L/b_K$$

Notice that since polymer molecular weight,  $M$ , is proportional to the number of its backbone units,  $n$ , the Kuhn length  $b_K$  is a constant when  $a$  is 0.5, but becomes a weak function of molecular weight when  $a$  is larger than 0.5. A nonconstant Kuhn step length allows us to account implicitly for the effect of excluded volume in a good solvent.

The next parameter to be determined is the bead drag coefficient  $\zeta$ . From the Zimm theory for a dilute polymer in a  $\Theta$  solvent, the “characteristic” relaxation time  $\tau_0$  can be related to the polymer intrinsic viscosity  $[\eta]_0$  and the longest relaxation time  $\tau_1$  by

$$\tau_0 = \frac{[\eta]_0 M \eta_s}{N_A k_B T} = \sum_{i=1}^{N-1} \tau_i = S \tau_1 \quad (15)$$

where  $\eta_s$  is the solvent viscosity, and  $N_A$  is Avogadro’s number. The constant  $S$  is 2.369 in a  $\Theta$  solvent and becomes somewhat smaller in a good solvent with a lower bound given by the Rouse value,  $S = 1.645$ . For PEO in water, we take  $S$  to be 2. Using eq 15, we estimate the longest relaxation time of PEO with molecular weight 1.4 million in water to be around  $1.5 \times 10^{-4}$  s. This estimated longest relaxation time is close to the measured one ( $\sim 1.0 \times 10^{-4}$  s) that Odell and Keller<sup>10</sup> obtained from the extension rate at which the intensity of flow-induced birefringence in a cross-slot device rises rapidly. Since our simulations neglect hydrodynamic interactions, the longest relaxation time of the simulated bead–spring chain obeys the Rouse theory, for which

$$\tau_1 = \frac{\zeta}{16k_B T \beta_s^2 \sin^2 \left( \frac{\pi}{2(N_s + 1)} \right)} \quad (16)$$

where  $\beta_s^2 = 3N_s/2\langle R^2 \rangle_0$  and  $N_s$  is the number of springs.

Because the bead drag coefficient must be chosen so that we can recover the correct longest relaxation time  $\tau_1$ , eq 15 should match eq 16, giving

$$\frac{[\eta]_0 M \eta_s}{S N_A k_B T} = \frac{\zeta}{16k_B T \beta_s^2 \sin^2 \left( \frac{\pi}{2(N_s + 1)} \right)} \quad (17)$$

Substituting eqs 12 and 13 into eq 17, we obtain

$$\zeta = 4N_s \sin^2 \left( \frac{\pi}{2(N_s + 1)} \right) A^{2/3} \kappa^{1/3} M^{(1+a)/3} S^{-1} N_A^{-1} \eta_s \quad (18)$$

**Simulation Details.** To solve the Brownian dynamics equations we use an explicit Euler’s integration

method. While several semiimplicit methods are more stable and more efficient than the explicit Euler's method, they are not suitable for the position-dependent velocity-gradient field used here. Moreover, since we want to capture accurately the instant in time that a chain scission event occurs, semiimplicit schemes with larger time steps are not suitable. To start a simulation, we first generate a random initial configuration with springs of length equal to the equilibrium spring length  $R_s = \sqrt{\langle R^2 \rangle_0 / N_s}$  and let the bead-spring model equilibrate under a no-flow condition for a period of 10 relaxation times. We then run the simulations under a steady shearing flow with a shearing rate that matches the shear rate in the inlet at a particular distance  $X$  from the wall so that the polymer molecules can reach their steady state in the channel before entering the cross-slot region. We shear at this rate for 100 strain units and then place the deformed chain at the desired position  $X \mu\text{m}$  from the channel wall at a location  $600 \mu\text{m}$  upstream from the center of the cross slot. The initial stretch of the chain will depend on its initial position relative to the center axis of the inlet channel, and will represent the steady-state distribution of chain configurations achieved in a long entry channel.

Once the chain is placed in the inlet channel, the velocity of the surrounding solvent at the position of each bead of the chain is extracted from the results of finite element simulation by using a bilinear interpolation method. We have checked the accuracy of the interpolation method by tracking the movement of a single particle in the cross-slot. The trajectory of the particle should match the streamline calculated from the finite element simulation. We found that the particle trajectories lie on the corresponding streamline over the entire geometry, except when the particle is initially placed  $1 \mu\text{m}$  from the wall in the upstream channel. In this case the particle hits the wall downstream at  $0.04 \mu\text{m}$  upstream from the corner while the streamlines calculated from the finite element method never hit the wall. We have improved the accuracy of our interpolation method by using a higher order, biquadratic interpolation function, but the tracking particle still hits the wall  $0.015 \mu\text{m}$  upstream of the corner. This divergence is probably caused by the very high velocity gradient around the corner and may be solved by using a finer mesh there. However, the computing time will be formidable for BD simulations in this situation. Instead of using a finer mesh, we found that the flux of polymer mass that passes through this region (within  $1 \mu\text{m}$  from the wall) is less than 0.01% of the total polymer flux (less than one part in 10000), so we choose to neglect the chain scission occurring between this streamline and the wall.

Because the cross-slot is symmetric in both the  $x$  and  $y$  directions, we only run the simulations in the one-fourth of the cross-slot geometry. To explore the position dependence of polymer degradation in the cross-slot, we assume that the concentration of polymer in the solution is homogeneous and release a chain every  $0.01 \mu\text{m}$  along the  $x$  direction across the inlet channel. The chains initially placed near the axis of the inlet channel sometimes diffuse to another region before entering the cross-slot region. We record the chain behavior and attribute its properties to the starting position of the chain relative to the inlet axis. In this study, all results are obtained from an ensemble of 14900 individual chains.

**Chain Scission Criterion.** All the chain scission studies with BD simulations have so far used either a critical stretch or a critical force as the criterion for the occurrence of breakage. However, the two kinds of criteria are equivalent since a stretch corresponds to a certain value of the spring force and vice versa. Following the earlier studies, we assume that a chain breaks when any spring bears a force over a preset critical spring force. This models the intuitively reasonable assumption that a polymer chain breaks when any part of it experiences a tension over its fracture strength. Odell and Keller<sup>10</sup> have estimated the C–C bond strength to be  $2.5 \sim 13.4 \text{ nN}$ . Nguyen and Kausch<sup>37</sup> compared estimates of the strength of the C–C bond from various sources which were all of the order of few nanonewtons. Knudsen et al.<sup>29</sup> matched the C–C bond dissociation energy to the FENE spring potential and derived a critical extension of a spring. However, the critical extension reported in that paper is wrong. We use their formula and parameters to calculate the correct critical spring extension and find that the corresponding spring force is around  $14 \text{ nN}$ . The recent measurement of the C–C bond strength using an atomic force microscope (AFM) reported a value of around  $4.1 \text{ nN}$ .<sup>38</sup> The same study also reported the C–O bond strength to be around  $4.3 \text{ nN}$ , which is very close to that of a C–C bond. Thus, we can assume that the PEO molecule has uniform bond strength along its backbone. In our study, we vary the critical spring force from 4 to  $0.5 \text{ nN}$  to investigate the influence of the critical spring force.

There are more sophisticated stochastic models in which a fracture probability per unit time is defined, such as the “thermal activated barrier to scission” (TABS) model.<sup>14</sup> The basic assumption of the TABS model is that chain scission occurs when thermal fluctuations overcome the energy barrier for bond dissociation. The role of the flow-induced tension along the chain is to reduce the energy barrier from its equilibrium state. The rate constant of scission can then be written as

$$k = v \exp[-(U - Fb)] \quad (19)$$

where  $v$  is a constant which includes the vibration frequency of the bond and the effect of temperature, and  $U$  is the dissociation barrier.  $F$  is the tension acting on the bond, and  $b$  is the length scale of a bond. With the TABS model, the probability of scission increases with the increasing tension. The use of a critical spring force thus amounts to approximating eq 19 by a step function that can be expressed as

$$k = 0 \quad \text{when } F < F_{s,c} \\ k = \infty \quad \text{when } F \geq F_{s,c} \quad (20)$$

where  $F_{s,c}$  is the critical spring force. Figure 4 shows a qualitative comparison between these two models. If we choose the critical spring force carefully, the total scission yield per pass through the geometry predicted using a critical spring force might not be very different from that predicted using TABS model. However, the TABS model will predict a broader fragment distribution because the scission rate is a continuous function of the imposed tension. In the future, such models can readily be incorporated into our Brownian dynamics code, once more scission experimental results are ob-

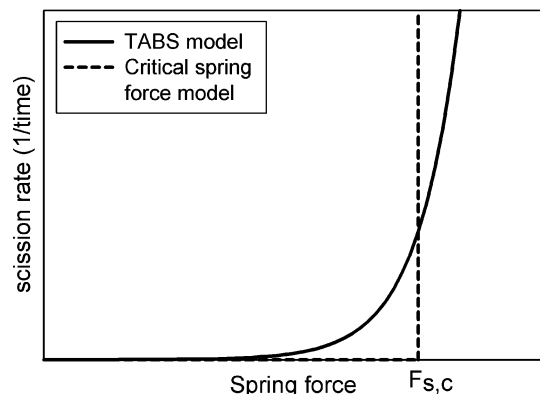


**Figure 4.** Qualitative comparison between the scission rate of the TABS model and that of the critical-spring-force model.

tained at low enough Reynolds number to be meaningfully compared quantitatively with our predictions.

Because we have neglected explicit incorporation of hydrodynamic interactions into the bead–spring model, the tension in the fully extended polymer PEO chain with  $M_w = 1.4$  million predicted by the model is less by a factor of around five than one would expect for a fully extended filament using the Batchelor formula.<sup>24</sup> Thus, the critical tension needed for breakage in the simulations will probably need to be adjusted downward by a similar factor, relative to the true value, if accurate chain scission predictions are to be obtained.

In our simulations, the fragments of a broken chain continue flowing with the fluid until they leave the cross-slot region and enter the exit channel where further chain scission is absent. Until they reach the exit channel, these fragments can break again, even multiple times, whenever the scission criterion is attained.

**Birefringence Calculations.** Since chain scission is a phenomenon that cannot be observed directly in the experiments, it is difficult to determine experimentally where the chains break in the flow cell. However, flow birefringence can be employed to provide an indication of the zones of high stress where chain breakage events are likely to be concentrated. Miles and Keller<sup>4</sup> observed a bright birefringent streak along the center plane of the exit channel of a cross-slot device. Gardner et al.<sup>5</sup> also reported a birefringence pattern in the entry channel of a cross-slot at a high flow rate. Thus, if we can predict accurately the flow birefringence observed in these experiments, we can demonstrate the reliability of our method of computing chain segmental orientation, which is a prerequisite to accurate prediction of scission.

For each “Kuhn” segment of a polymer chain, the polarizability tensor  $\alpha$  can be expressed as<sup>39</sup>

$$\alpha_i = \alpha_2 I + (\alpha_1 - \alpha_2) u_i u_i \quad (21)$$

where  $\alpha_1$  and  $\alpha_2$  are the polarizabilities along, and perpendicular, to the segment, respectively;  $u_i$  is a unit vector along the direction of the  $i$ th Kuhn segment. For a bead–rod chain, since each rod represents a Kuhn segment, the polarizability tensor of a segment is given by eq 21 and the polarizability tensor of the whole chain is just the summation of the polarizability tensors for all the segments. However, for a bead–spring model, a

spring usually represents 10 or more Kuhn segments, so the polarizability tensor for each spring should be given by the summation of the polarizability tensors over all Kuhn segments that the spring represents.<sup>23</sup> That is

$$\alpha_i \approx \alpha_2 \sum_{j=1}^{N_{K,s}} I + (\alpha_1 - \alpha_2) \sum_{j=1}^{N_{K,s}} u_j u_j \quad (22)$$

where  $j$  represents the  $j$ th Kuhn segment in the  $i$ th spring, and  $N_{K,s}$  is the number of Kuhn segments per spring. Once the polarizability tensor is known, the index of refraction  $n$  can be expressed by the Lorentz–Lorenz formula, and it can be linearized as

$$n_i \approx \frac{4\pi}{3} \frac{(n_0^2 + 2)^2}{6n_0} \alpha_i \quad (23)$$

where  $n_0$  is the refractive index of the solvent. Since we are only interested in the anisotropy of the birefringence tensor  $\tilde{n}$ , we can drop the isotropic part, giving

$$\begin{aligned} n_i &\approx \frac{4\pi}{3} \frac{(n_0^2 + 2)^2}{6n_0} (\alpha_1 - \alpha_2) \sum_{j=1}^{N_{K,s}} u_j u_j \\ &= \frac{4\pi}{3} \frac{(n_0^2 + 2)^2}{6n_0} (\alpha_1 - \alpha_2) N_{K,s} \sum_{j=1}^{N_{K,s}} \frac{u_j u_j}{N_{K,s}} = C \sum_{j=1}^{N_{K,s}} \frac{u_j u_j}{N_{K,s}} \end{aligned} \quad (24)$$

where the constant is given by

$$C = \frac{4\pi}{3} \frac{(n_0^2 + 2)^2}{6n_0} (\alpha_1 - \alpha_2) N_{K,s} \quad (25)$$

In a bead–spring chain, we do not know the exact configurations of the Kuhn segments in a spring, so the instantaneous value of  $\sum_{j=1}^{N_{K,s}} u_j u_j / N_{K,s}$  cannot be calculated directly from the simulations. We can, however, assume that each spring represents a microcanonical ensemble and the Kuhn steps represented by the spring sample their equilibrium distributions of orientations subject to a fixed spring vector. We thereby obtain the average value of  $\sum_{j=1}^{N_{K,s}} u_j u_j / N_{K,s}$  as a function of the stretch ratio  $\lambda$  of the spring. In this way, Li and Larson<sup>23</sup> developed the following formula

$$n_i \approx C \sum_{j=1}^{N_{K,s}} \frac{u_j u_j}{N_{K,s}} = C \begin{bmatrix} T_{11} & T_{12} & T_{13} \\ T_{21} & T_{22} & T_{23} \\ T_{31} & T_{32} & T_{33} \end{bmatrix}_i \quad (26)$$

where



1,2,3:*x,y,z* directions, respectively

$$\begin{aligned}
 T_{11,i} &= [C^2 f_{xx} + S^2 f_{yy}]_i \\
 T_{12,i} &= T_{21,i} = [CSc(f_{xx} - f_{yy})]_i \\
 T_{13,i} &= T_{31,i} = [CSs(f_{xx} - f_{yy})]_i \\
 T_{22,i} &= [S^2 c^2 f_{xx} + C^2 c^2 f_{yy} + s^2 f_{yy}]_i \\
 T_{23,i} &= T_{32,i} = [cs(f_{xx} - f_{yy})]_i \\
 T_{33,i} &= [S^2 s^2 f_{xx} + C^2 s^2 f_{yy} + c^2 f_{yy}]_i \\
 f_{xx} &= \frac{1}{3} + \frac{2}{5}\lambda_i^2 + \frac{2}{15}\lambda_i^4 + \frac{2}{15}\lambda_i^6 \\
 f_{yy} &= \frac{1}{3} - \frac{1}{5}\lambda_i^2 - \frac{1}{15}\lambda_i^4 - \frac{1}{15}\lambda_i^6 \\
 C &= \cos \theta, \quad S = \sin \theta \\
 c &= \cos \phi, \quad s = \sin \phi \\
 \theta &= \tan^{-1}(\sqrt{r_{iy}^2 + r_{iz}^2}/r_{ix}) \\
 \phi &= \tan^{-1}(r_{iz}/r_{iy})
 \end{aligned} \quad (27)$$

where  $r_{ix}$ ,  $r_{iy}$ ,  $r_{iz}$  are the  $x$ ,  $y$ , and  $z$  components of the  $i$ th spring vector. Because of the planar symmetry of the flow, we can reduce the refraction index tensor from 3rd order to 2nd order,

$$\begin{aligned}
 n_i &= \begin{bmatrix} n_{11} & n_{12} \\ n_{21} & n_{22} \end{bmatrix} = C \begin{bmatrix} T_{11} & T_{12} \\ T_{21} & T_{22} \end{bmatrix} \\
 &\approx \begin{bmatrix} n_{11} & n_{12} \\ n_{21} & n_{22} \end{bmatrix}
 \end{aligned} \quad (28)$$

The birefringence  $\Delta n$  and the extinction angle  $\chi$  are

$$\Delta n = \sqrt{(n_{11} - n_{22})^2 + 4n_{12}^2} / (n_{11} - n_{22}) \quad (29)$$

$$\chi = \frac{1}{2} \cos^{-1} \left( \frac{n_{11} - n_{22}}{\Delta n} \right) \quad (30)$$

Since we have a planar flow,  $\phi \sim 0$ . If  $\lambda_i$  is unity (fully stretched) at any  $\theta$ , we can calculate the maximum birefringence as  $|\Delta n| = C$ .

### III. Results and Discussion

**Flow Birefringence Simulations.** In Figure 5, we present the contour plots of the flow-induced birefringence, normalized by the value for fully stretched chains, calculated from BD simulations in the cross-slot device. To obtain this pattern, we suppressed chain breaking in this set of simulations. Figure 5a was generated at  $Re = 4.5$  and  $De = \tau_1 \dot{\epsilon}_{nominal} = 75$ , while  $Re = 0.45$  and  $De = 7.5$  for Figure 5b. As can be seen in Figure 5a, a very strong birefringent line appears along the center line of the exit channel (zone 1) as expected at high flow rate. However, there is another, unexpected, strong birefringent zone shown at the corner of the cross-slot (zone 2). Furthermore, a bright birefringence pattern also appears along the walls of inlet and exit channels (zone 3). The birefringence in zone 1 is no doubt caused by the strong elongational flow near the stagnation point. When the fluid approaches the stagnation point, it must reduce its speed to nearly zero and then accelerate once it passes the stagnation point.

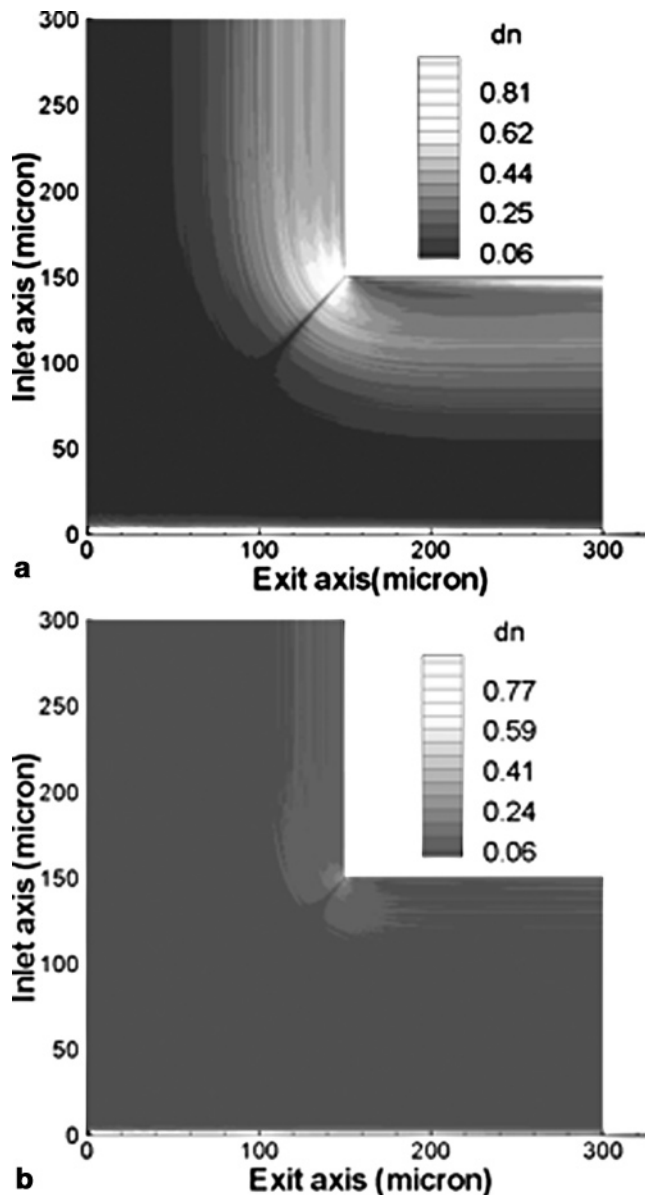


**Figure 5.** Simulated flow birefringence magnitude normalized by the birefringence of fully stretched chains of PEO in dilute aqueous solutions in a planar cross-slot flow at (a)  $Re = 4.5$  and  $De = \tau_1 \dot{\epsilon}_{nominal} = 75$ , and (b)  $Re = 0.45$  and  $De = 7.5$ .

This process results in a strong extensional flow that stretches the chain and produces a strong birefringence.

The birefringence shown in zone 3 is caused by the strong shear flow along the channel wall. The Weissenberg number  $Wi_{shear} = \dot{\gamma} \tau_1$  at the wall can be estimated to be around 200. Although the shear rate is very high, the polymer is not likely to break since the shear flow makes it tumble, so that it does not become fully stretched. Both experiments<sup>17</sup> and simulations<sup>31,40</sup> show that in a shear flow, the average normalized polymer extension reaches an asymptotic value of around 0.4–0.5 at high Weissenberg number. Therefore, a medium-strength birefringence is induced in this region.

The birefringence shown in zone 2 results from the strong shear flow followed by the elongational flow at the corner. The polymer molecules are partially stretched by the strong shear flow near the channel walls and then further stretched when they pass near the corner where an elongational flow component exists. Farinato<sup>41</sup> studied flow birefringence of dilute aqueous poly(styrene

sodium sulfonate) solutions in a cross-slot and observed a weak birefringence region along the walls of the inlet and exit channels in addition to a strong birefringence pattern at the stagnation point at the center of the device. The study also reported that this wall birefringence grows with increasing flow rate but remains weaker than at the center of the flow cell. Notice that Figure 5 plots contours of the absolute value of the birefringence. The birefringence is negative in the inlet channel and positive in the exit channel (for molecules with a positive value of  $\alpha_1 - \alpha_2$ ) because the polymer chains are stretched in the  $y$  direction in the inlet channel and in the  $x$  direction in the exit channel. Also in Figure 5a, there is a  $45^\circ$  line intersecting the corner along which there is no birefringence, because the polymer molecules there are oriented on average at  $45^\circ$ , as they are rotating between the inlet and outlet orientations.

While we have predicted three birefringence regions in our simulations, most experiments report only a single bright birefringent streak running from the stagnation point outward along the center plane of the exit channel. The flow birefringence measurements cited above were made at the flow rate at which a bright birefringent line along the center line first appears. From the study of Odell and Keller,<sup>10</sup> we estimate that the flow rate at which chain scission occurs is roughly 50 times higher than the minimum flow rate able to induce flow birefringence for a PEO–water solution with molecular weight 1.4 million. In other words, the flow birefringence patterns in most experiments were probably obtained for elongational flows strong enough to cause the polymer coils to undergo the coil–stretch transition but not nearly strong enough to induce chain scission.

To check this explanation, we performed another set of simulations at a flow rate 10 times lower than the previous one, low enough to avoid chain scission for reasonable values of the critical extension for scission, and plot the results in Figure 5b. The Reynolds number in Figure 5b is  $Re = 0.45$  and  $Wi_{\text{shear}}$  near the channel walls is around 20. As shown in Figure 5b, the birefringence along the center line of the exit plane is still bright, but the birefringence near the walls has become dim. Thus, we believe that the birefringence pattern in Figure 5b corresponds more closely to the birefringence experiments than does that of Figure 5a. However, the pattern in Figure 5a represents better the birefringence at flow conditions required to induce chain scission.

**Molecular Weight Distribution of PEO Fragments after Scission.** Figure 6 shows the molecular weight distribution of PEO fragments after one pass through the cross-slot device at a Reynolds number  $Re = 4.5$  with different critical spring forces for scission. We plot only the mass distribution of scission products and omit the unbroken molecules. To produce this plot, we assume that the concentration of PEO is homogeneous everywhere in the flow cell. We place one bead–spring chain every  $0.01 \mu\text{m}$  across the inlet from  $x = 0 \mu\text{m}$  (center) to  $x = 149 \mu\text{m}$  (wall) and obtain the scission yield in one pass. Since the flux of polymer is not uniform across the channel due to the parabolic velocity profile, we use the flux of fluid at each inlet position as a weighting factor when we count the scission contribution to the total scission yield. As can be seen in Figure 6, when the critical spring force is set to be  $F_{s,c} = 4 \text{ nN}$ , the elongation rate is barely high enough to break few

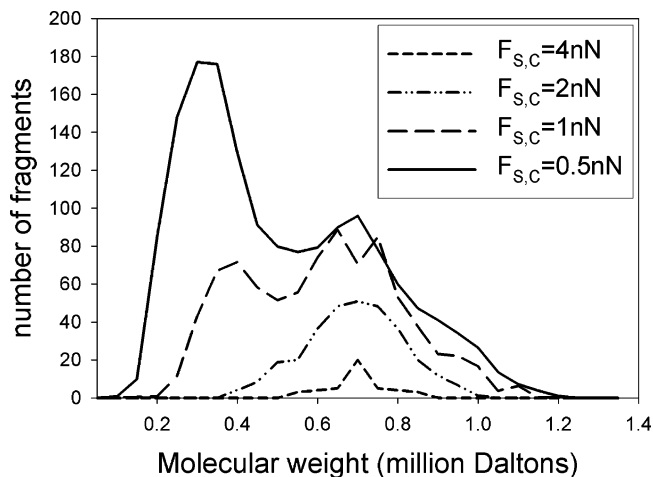


**Figure 6.** Simulated molecular weight distribution of polymer fragments after chain scission in one pass through the cross-slot device. The molecular weight of an intact PEO molecule is taken to be  $M_w = 1.4 \times 10^6$ .

chains, and a very low degradation yield is observed. The fragments of PEO symmetrically distribute around a molecular weight equal to half that of an intact PEO molecule. When the critical spring force is reduced to  $F_{s,c} = 2 \text{ nN}$ , we observe a higher scission yield and a broader distribution of scission fragments. However, midpoint scission is again observed at this critical force. When we further reduce the critical spring force to  $F_{s,c} = 1 \text{ nN}$ , the scission yield rises even higher, as expected. In this case, in addition to the midpoint scission peak at  $M_w = 0.7$  million, a second peak appears at  $M_w \sim 0.35$  million, which is one-quarter of the molecular weight of an intact PEO molecule. When the critical spring force  $F_{s,c}$  decreases to  $0.5 \text{ nN}$ , the peak at  $M_w = 0.7$  million shrinks and the peak at  $0.35$  million becomes higher than that at  $M_w = 0.7$  million. In Figure 6, we therefore predict the phenomenon of chain halving and quartering previously reported in experiments by Odell et al. and Nguyen et al.

**Where in the Flow Cell Does Chain Scission Occur?** Whether a chain breaks or not is determined by two factors: (1) the magnitude of the imposed elongation rate and (2) the cumulative strain imposed at a strain rate sufficiently high to cause polymer stretch and eventual breakage. On the basis of these two criteria, previous experimental and theoretical investigators studying cross-slot flow have assumed that chain scission takes place only along and close to the center line of the geometry. The argument for this localization is that the flow is slow and purely elongational near the center line, and so the chains confined to this region have longer residence time (and thus accumulate enough Hencky strain) to reach their fully stretched length. Outside this region, polymer molecules will not accumulate enough elongational strain even though the elongation rate might be higher than needed to break a fully extended chain. On the other hand, the flow near the wall is dominated by a strong shearing component. Since it is well-known that shearing flow causes polymer molecules to tumble, which prevents complete stretching, even a very strong shearing flow is not likely to break a polymer chain.<sup>42</sup>

As we have shown in Figure 5, parts a and b, at a low flow rate, the flow birefringence only appears along the center line of the exit plane; however, at a higher flow rate, at which chain scission occurs, a strong

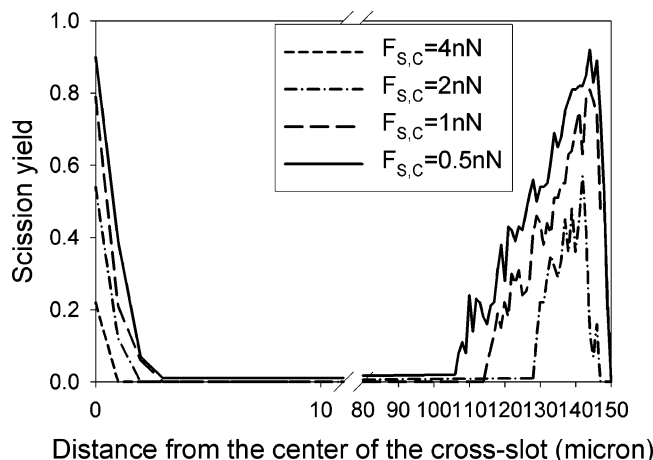


**Figure 7.** Simulated scission yield vs distance of the injection point from the center axis of the injection channel.

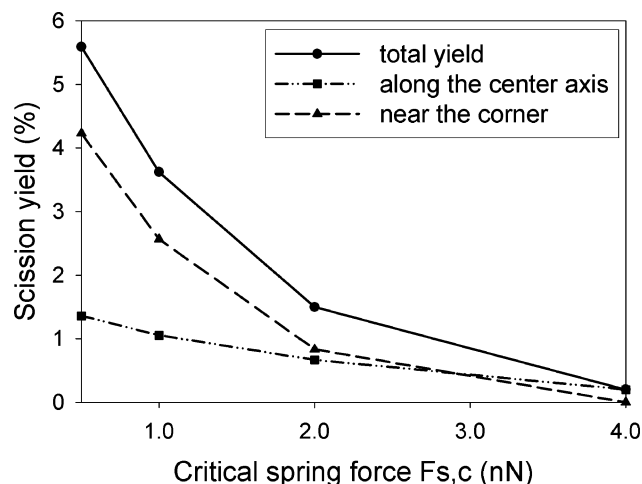


**Figure 8.** Simulated overall scission yield vs the critical spring force  $F_{s,c}$  and yield from scission near the walls and near the center line.

birefringence pattern also appears near the channel walls. If strong birefringence is an indicator of the occurrence of chain scission, does the strong birefringence near the wall imply that chain scission occurs near the wall?

Figure 7 shows how the polymer scission yield changes as a function of injection distance from the centerline. The results shown here are obtained using the same method as in the previous section, so that we can determine the locations in the cross-slot geometry at which chain scission is most likely to occur. As can be seen in Figure 7, except for the case in which the bond strength ( $F_{s,c} = 4$  nN) is so high that the flow is barely strong enough to break any chains at all, more chains break near the wall than along the center line of the cross-slot. This conclusion is supported by Figure 8 which plots the total scission yield vs critical spring force along with the portion of the scission yield resulting from breakage along the center axis and from breakage near the corner. From Figure 8, we also find that an even higher fraction of the scission occurs along the wall when the critical spring force is decreased.

The results shown here obviously contradict the assumptions made in previous studies of chain-scission in cross-slot devices, but are consistent with our birefringence simulations. BD simulations have shown that preshearing can help a polymer chain unravel faster in

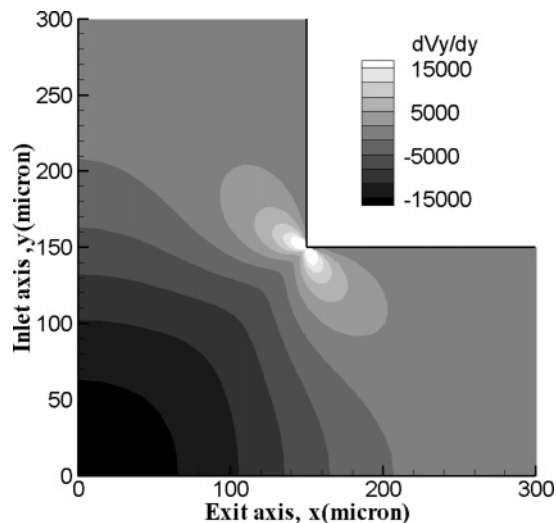


**Figure 9.** Simulated velocity gradient  $\partial V_y/\partial y$  in the planar cross-slot flow.

a subsequent elongational<sup>32</sup> flow and we believe that the same phenomenon accounts for our observation of chain scission near the wall.

To better explain this phenomenon, we present a contour plot of the velocity gradient  $\partial V_y/\partial y$  in Figure 9. Since the simulated flow is two-dimensional,  $\partial V_x/\partial x$  is just the negative of  $\partial V_y/\partial y$ . In Figure 9, the dark area represents the region of the flow that is compressional in the  $y$  direction but elongational in the  $x$  direction, while the light region represents that the flow is elongational in the  $y$  direction but compressional in the  $x$  direction. The chains flowing along the center line experience no shearing or elongational flow before moving into the cross-slot region. As they approach the stagnation point, they experience a strong elongational flow component in the  $x$  direction and start to extend. However, only when the chains undergo a coil–stretch transition are they able to reach the fully stretched state and then break. For PEO with molecular weight  $M_w = 1.4 \times 10^6$ , in a fast elongational flow, a strain of around 4.5 Hencky units is needed for the chain to reach its fully stretched state from the coiled state [e.g. for a PEO with  $M_w = 1.4 \times 10^6$ , the ratio between the contour length and the equilibrium coil size is 93, implying a minimum Hencky strain of  $\ln(93) = 4.5$  units]. As the chains pass through the stagnation point, they continue to experience an elongational flow in the  $x$  direction. If they reach the fully stretched state before leaving the region with a high elongation rate, they can break.

The chains moving along the wall, as mentioned before, are prestretched by the strong shearing flow in the  $y$  direction and then enter a zone with a strong elongational flow also in the  $y$  direction. Since the shearing flow and the subsequent elongational flow stretch the chains in the same direction, some of these chains reach their fully stretched state and thus break. Once the chains turn around the corner, they are still highly stretched, but now oriented in the  $x$  direction, while the flow continues to stretch them in the  $y$  direction (see Figure 9), and therefore compress them (or reduce their stretch) in the  $x$  direction. As a result, the chains will break in the inlet channel but not in the outlet channel. We plot the exact positions where individual chains break in Figure 10 for the case in which the critical spring force is set to 1 nN. Each point represents one scission event. As can be seen, chain



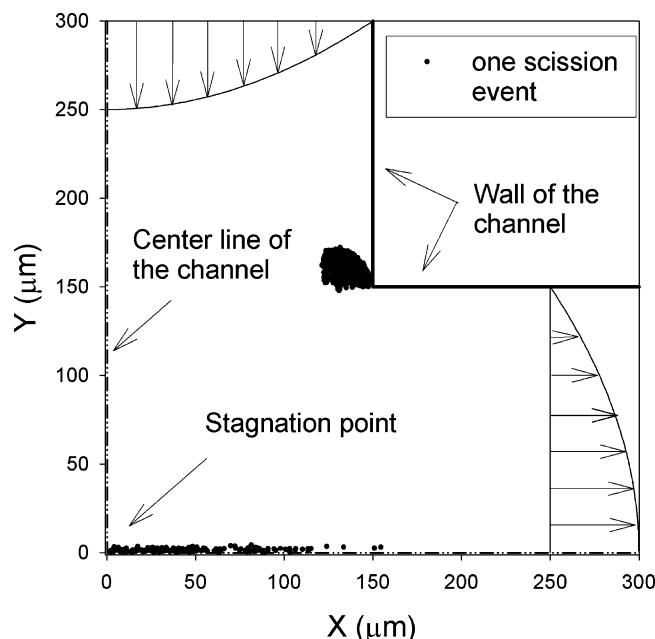


**Figure 10.** Positions at which chain scission occurs in the simulations for a critical spring force of 1 nN. Each point represents one scission event.

scission occurs along the center line of the exit channel and near the corner of the cross-slot before the chains flow into the outlet channel.

Chains that are neither close to the center line nor close to the walls do not experience the required combination of elongational and shear strain for them to extend. This is why there is no chain scission in the large area between the center line and the walls of the cross-slot device.

**Comparison with Experiments.** This study is not intended to predict quantitatively the experimental data of Odell and Keller,<sup>10</sup> since the flow rate in their device was high enough to produce turbulence, while we assume a laminar flow field in our simulations. However, we still capture some key features observed in the experiments. For a critical spring force of 2 nN, the simulations show that PEO molecules with a molecular weight  $M_w = 1.4 \times 10^6$  degrade to molecules with molecular weight  $M_w = 0.7 \times 10^6$ , which is consistent with the observations of Odell and Keller. The scission yield is around 1.6% in one pass in our simulations while Odell and Keller reported a yield of  $\sim 2.5\%$  per pass. Considering that the critical spring force we used, the midpoint scission we obtained, and the scission yield we observed are all consistent with experimental data, we conclude that our BD simulations with a bead-spring model have demonstrated the potential eventually to predict quantitatively flow-induced polymer chain-scission. Further experimental studies of this phenomenon in well-defined laminar flows are strongly encouraged.

#### IV. Conclusions

By using Brownian dynamics simulations with a Newtonian flow field generated by a finite-element method, we have simulated birefringence and flow-induced chain scission in a planar cross-slot flow. The Brownian dynamics simulations capture the chain halving and chain quartering observed in experiments and also predict unexpectedly that chain scission occurs not only along the center outflow axis but also near the

corners of the cross-slot. Although no direct evidence can verify our prediction, the predicted flow birefringence matches the report of Farinato<sup>41</sup> regarding the appearance of wall birefringence in the cross-slot flow. The preshearing caused by the strong shearing flow near the channel walls helps the chains unravel and thus break in the subsequent elongational flow. As a result, as the flow rate increases, a higher fraction of scission will occur near the wall rather than along the center axis.

**Acknowledgment.** The work was supported by the Defense Advanced Research Projects Agency (DARPA), Advanced Technology Office, Friction Drag Reduction Program (ARPA Order No.: N621/00. Issued by: DARPA/CMO. Grant No.: MDA972-01-0010). The authors thank Prof. Michael J. Solomon and Mr. Siva A. Vanapalli for valuable discussions.

#### Appendix: Assessment of the Effects of Hydrodynamic Interactions on Simulations of Chain Scission

Intramolecular hydrodynamic interaction has been shown to have a strong influence on the nonlinear behavior of a polymer chain.<sup>24,31,43</sup> A detailed comparison of the evolution of the polymer chain configurations in simulations also shows that HI retards the unraveling of a chain in a strong extensional flow.<sup>31</sup> Therefore, including HI is necessary if one wants to obtain a quantitatively accurate prediction on chain scission. However, we are forced to perform the BD simulations without HI because of current limits on computational power. The reasons that inclusion of HI is so difficult for simulations of chain scission, and the ways in which neglect of HI are likely to affect the predictions of birefringence and chain scission, are discussed in this appendix.

Many studies have used BD simulations to investigate the qualitative effect of HI in dilute polymer solutions, but attempts to make quantitative predictions have only very recently been made, including the work of Jendreck et al.<sup>44</sup> for DNA, and Hsieh et al.<sup>24,31</sup> for polystyrene and DNA. Among these quantitative studies, only the work of Hsieh et al. obtained all simulation parameters a priori from the drag properties of the polymer in the fully stretched state (where scission is most likely) and examined their method by comparing the simulated polymer stresses to the experimentally measured ones. The predicted stresses for polystyrene in a uniaxial extensional flow are in a good agreement with the measured ones<sup>45</sup> from low to medium strains. However, the method fails to predict the stress accurately at high strains, possibly due to chain scission at high strains.

Even if the method of Hsieh et al.<sup>24</sup> could in principle be made accurate over the whole range of stretch up to full extension (perhaps by incorporating chain scission), the available of computer power is not yet sufficient to carry out these simulations with full HI. The work of Hsieh et al.<sup>24</sup> shows that we can currently barely afford to use about 160 beads per chain in an ensemble of 100 chains. However, scaling rules developed in that same work, when applied to PEO, indicate that 240 beads would be needed to simulate accurately PEO chain with molecular weight of 1.4 million. (This large number of beads needed is estimated by assuming that the hydro-



dynamic interaction parameter  $h^*$  is set to a value of 0.25.) In addition, since the predictor–corrector method, which is the fastest available numerical scheme for BD simulations with the bead–spring model, is not suitable for simulations with position-dependent flow gradients, the speed of the simulation in a cross-slot flow will be lessened by a factor of 10 or more. Considering this large number of beads we would need to use, the more time-consuming numerical scheme, and the huge ensemble required for scission simulations (15000 runs in this work comparing to 100 runs in Hsieh et al.<sup>24</sup>), we cannot afford to include HI over the whole flow field used in the simulations in this study.

Neglecting HI will have several important consequences, but as we consider the consequences of neglect of HI, we are led to the conclusion that the qualitative picture of chain scission that we have presented here will not be altered. The first consequence of neglect of HI shows up in the choice of value of the drag coefficient. As is well understood, the behavior of a long-chain polymer is dominated by HI in the coiled state and approaches a free-draining limit in the fully stretched state. As a result, although the local drag coefficient reflecting the relationship between drag force and *local* velocity remains constant for a chain undergoing stretch, the apparent drag coefficient reflecting the relationship between drag force and the *macroscopic* velocity field will change due to the change in the strength of the hydrodynamic shielding as the chain is stretched. As a result, the molecular weight dependence of the apparent drag coefficient will follow the Zimm theory in the coiled state and Rouse theory in the fully extended state. If HI is explicitly incorporated in the simulations, this change in apparent drag coefficient will be generated naturally by the simulations. However, since including HI in our simulations is too expensive, we must choose the bead drag coefficient based on either the coiled state or the fully stretched state. As discussed in text, we have chosen to set the drag coefficient by matching the longest relaxation time predicted by Zimm theory to that of the Rouse model so that we can reproduce the correct polymer behavior at small deformation without inclusion of HI. This choice was made so that, in the unstretched limit, the drag forces on our simulated chains will be similar to those on a chain with HI. As a result of this choice in our simulations, the coil–stretch transition will occur at a quantitatively correct velocity gradient. This is important since the coil–stretch transition leads to a strong jump in the birefringence. Because the birefringence is relatively insensitive to the change in the stretch for a moderately stretched chain, a correct prediction of the coil–stretch transition leads to a correct prediction of birefringence.

The disadvantage of this method is that the simulated spring forces in a fully stretched chain will be underestimated, since the increase in effective drag coefficient that occurs when chains stretch is not modeled. More seriously, our method will alter the molecular weight dependence of the critical spring force shift from  $\dot{\epsilon}_f \propto M_w^{-2}$  to  $\dot{\epsilon}_f \propto M_w^{-1.5}$  in a uniaxial extensional flow. To demonstrate this, we take the eq 5 from the Odell and Keller,<sup>10</sup> which describes the fracture force in an extensional flow as

$$F_f \propto \zeta \dot{\epsilon} N^2 \quad (\text{A-1})$$

If the drag coefficient  $\zeta$  is constant, and the number of

beads,  $N$ , is proportional to the molecular weight, we obtain

$$\dot{\epsilon}_f \propto M_w^{-2} \quad (\text{A-2})$$

However, since we match the longest relaxation time predicted by Zimm theory to that of Rouse model, the drag coefficient is no longer a constant but a function of molecular weight. From eq 18, we have

$$\zeta \propto \frac{M_w^{(1+\alpha)/3}}{N} \quad (\text{A-3})$$

Here, we assume  $N \gg 1$ . If we also take  $N$  proportional to the molecular weight and assume that  $\alpha$  is 0.5 as in a  $\Theta$  condition, we obtain

$$\zeta \propto M_w^{-0.5} \quad (\text{A-4})$$

Substituting (A-4) into (A-1), we have

$$\dot{\epsilon}_f \propto M_w^{-1.5} \quad (\text{A-5})$$

Obviously, our method will give a correct prediction of the polymer behavior for coils that have not yet undergone the coil–stretch transition, as well as a correct prediction of the birefringence, but will give a wrong scaling law of the critical strain rate for chain scission vs the polymer molecular weight. If one wants to obtain more accurate results when chains are fully stretched, one could choose to determine the drag coefficient by matching Batchelor's formula for the drag force acting on a slender rod, as we have done in previous work.<sup>23</sup> However, this will lead to an inaccurate prediction of the coil–stretch transition and of the birefringence. Despite the incorrect prediction of the scaling of the critical strain rate for scission on molecular weight, for any given molecular weight, the correct condition for scission could be obtained by adjusting the critical tension for scission downward with increasing molecular weight to compensate for the underprediction of chain tension that we suffer as a result of neglecting HI and choosing the bead drag coefficient based from the Zimm theory. Of course, in cases where the fragments resulting from a broken chain are themselves prone to break, this method of correction will fail.

In addition to the dilemma of determining an appropriate bead drag coefficient, neglecting HI is likely to raise another inaccuracy in our simulations. Using BD simulations, Hsieh and Larson<sup>31</sup> have shown that HI retards the unraveling of a chain in a strong extensional flow. Therefore, a chain unfolds more slowly and thus may break less readily in the presence of the HI. Hence, the presence of HI is expected to reduce the scission yield and to cause a broader distribution of fragments.

To check qualitatively for the effects of HI on the chain scission simulations, we perform two sets of simulations with HI with 40 bead-chains. One set of simulations is performed for the molecules flowing along the center line (0–1  $\mu\text{m}$  from the center line), and another set is performed for those flowing close to the wall (9–10  $\mu\text{m}$  from the wall). Each set is an ensemble of 100 runs, the same as in the simulations without HI. The hydrodynamic interaction effect is described by the Rotne–Prager tensor.<sup>46</sup> The hydrodynamic interaction parameter  $h^*$  is set to be 0.4589 and is determined by the method proposed by Hsieh et al.<sup>24</sup> by matching the

drag force estimated from Batchelor's formula to a bead-spring model. Notice that  $h^*$  mentioned here is actually  $h^*_{\max}$  in Hsieh et al.<sup>24</sup> The use of a  $h^*$  larger than 0.25 compensates partially for the use of small number of beads so that we can ensure that the simulated chain will experience the same drag force as a chain with 240 beads and  $h^* = 0.25$  does. The reader should bear in mind that the magnitude of HI in the simulation chains is still weaker than what we estimated for the corresponding PEO molecule. Therefore, the simulations with HI here do not give accurate predictions of the longest relaxation time and linear viscoelastic properties, but come closer to predicting them than do simulations that completely neglect HI. A detailed investigation of the effects of number of beads and choice of parameter  $h^*$  can be found in Hsieh and Larson.<sup>31</sup>

The chain scission simulations with HI follow the same procedure as those without HI. We preshear the chains to ensure the polymer molecules reaching their steady state in the channel before entering the cross-slot region. Since the drag force acting on half of the fully extended molecule at steady state in an extensional flow is increased by a factor of 4.597 when HI is incorporated, we raise the critical spring force correspondently from 1 to 4.597 nN to counteract this change. The simulation results show that the chains still break both along the center and near the wall with high, albeit somewhat reduced, scission yield. For chains released between 9 and 10  $\mu\text{m}$  from the wall the scission yield is down from 70% in the simulations without HI to 53% with HI while for those released within 1  $\mu\text{m}$  from the centerline the corresponding scission yield is down from 79% to 63%. The molecular weight distribution of fragment is broader with HI than is obtained in simulations without HI while the signature of chain halving and quartering remains unaffected. These results are consistent with our expectations based on the slower unraveling dynamics expected when HI is present.

## References and Notes

- (1) Moussa, T.; Tiu, C. *Chem. Eng. Sci.* **1994**, *49*, 1681.
- (2) Yu, J. F. S.; Zakin, J. L.; Patterson, G. K. *J. Appl. Polym. Sci.* **1979**, *23*, 2493.
- (3) Buchholz, B. A.; Zahn, J. M.; Kenward, M.; Slater, G. W.; Barron, A. E. *Polymer* **2004**, *45*, 1223.
- (4) Miles, M. J.; Keller, A. *Polymer* **1980**, *21*, 1295.
- (5) Gardner, K.; Pike, E. R.; Miles, M. J.; Keller, A.; Tanaka, K. *Polymer* **1982**, *23*, 1435.
- (6) Odell, J. A.; Keller, A.; Miles, M. J. *Polym. Commun.* **1983**, *24*, 7.
- (7) Merrill, E. W.; Horn, A. F. *Polym. Commun.* **1984**, *25*, 144.
- (8) Horn, A. F. *Nature (London)* **1984**, *312*, 140.
- (9) Keller, A.; Odell, J. A. *Colloid Polym. Sci.* **1985**, *263*, 181.
- (10) Odell, J. A.; Keller, A. *J. Polym. Sci., Part B: Polym. Phys.* **1986**, *24*, 1889.
- (11) Nguyen, T. Q.; Kausch, H. H. *J. Non-Newtonian Fluid Mech.* **1988**, *125*.
- (12) Nguyen, T. Q.; Kausch, H. H. *Polymer* **1992**, *33*, 2611.
- (13) Islam, M. T.; Vanapalli, S. A.; Solomon, M. J. *Macromolecules* **2004**, *37*, 1023.
- (14) Odell, J. A.; Keller, A.; Rabin, Y. *J. Chem. Phys.* **1988**, *88*, 4022.
- (15) Rabin, Y. *J. Chem. Phys.* **1987**, *86*, 5215.
- (16) Ryskin, G. *J. Fluid Mech.* **1987**, *178*, 423.
- (17) Smith, D. E.; Babcock, H. P.; Chu, S. *Science* **1999**, *283*, 1724.
- (18) Larson, R. G.; Hu, H.; Smith, D. E.; Chu, S. *J. Rheol.* **1999**, *43*, 267.
- (19) Reese, H. R.; Zimm, B. H. *J. Chem. Phys.* **1990**, *92*, 2650.
- (20) Atkins, E. D. T.; Taylor, M. A. *Biopolymers* **1992**, *32*, 911.
- (21) Kalashnikov, V. N.; Tsiklauri, M. G. *J. Non-Newtonian Fluid Mech.* **1993**, *48*, 215.
- (22) Li, L.; Larson, R. G.; Sridhar, T. *J. Rheol.* **2000**, *44*, 291.
- (23) Li L.; Larson R. G. *Rheol. Acta* **2000**, *39*, 419.
- (24) Hsieh, C. C.; Li L.; Larson, R. G. *J. Non-Newtonian Fluid Mech.* **2003**, *113*, 147.
- (25) López Cascales, J. J.; García de la Torre, J. *Chem. Phys.* **1991**, *95*, 9384.
- (26) López Cascales, J. J.; García de la Torre, J. *Chem. Phys.* **1992**, *97*, 4549.
- (27) Knudsen, K. D.; Hernández Cifre, J. G.; López Cascales, J. J.; García de la Torre, J. *Macromolecules* **1995**, *28*, 4660.
- (28) Knudsen, K. D.; Hernández, J. G.; García de la Torre, J. *Macromolecules* **1996**, *29*, 3603.
- (29) Knudsen, K. D.; Hernández, J. G.; García de la Torre, J. *Colloid Polym. Sci.* **1997**, *275*, 1001.
- (30) Knudsen, K. D.; Lopez Martinez, M. C.; García de la Torre, J. *Biopolymers* **1996**, *39*, 435.
- (31) Hsieh, C. C.; Larson, R. G. *J. Rheol.* **2004**, *48*, 995.
- (32) Larson, R. G. *J. Non-Newtonian Fluid Mech.* **2000**, *94*, 37.
- (33) Crochet, M. J.; Davies, A. R.; Walters, K. *Numerical simulation of non-Newtonian flow*; Elsevier: Amsterdam, 1984.
- (34) Cohen, A. *Rheol. Acta* **1991**, *30*, 270.
- (35) Larson, R. G. *The Structure and Rheology of Complex Fluids*; Oxford University Press: New York, 1999.
- (36) Virk, P. S. *AIChE J.* **1975**, *21*, 625–656.
- (37) Nguyen, T. Q.; Kausch, H. H. *Adv. Polym. Sci.* **1992**, *100*, 73–182.
- (38) Grandbois, M.; Beyer, M.; Reif, M.; Clausen-Schaumann, H.; Gaub, H. E. *Science* **1999**, *283*, 1727–1730.
- (39) Fuller, G. G. *Optical Rheometry of Complex Fluids*; Oxford University Press: New York, 1995.
- (40) Hur, J. S.; Shaqfeh, E. S. G.; Larson R. G. *J. Rheol.* **2000**, *44*, 713.
- (41) Farinato, R. S. *Polymer* **1988**, *29*, 160.
- (42) Odell, J. A.; Muller, A. J.; Narh, K. A.; Keller, A. *Macromolecules* **1990**, *23*, 2.
- (43) Schroeder, C. M.; Babcock, H. P.; Shaqfeh, E. S. G.; Chu, S. *Science* **2003**, *301*, 1515.
- (44) Jendrejack, R. M.; de Pablo, J. J.; Graham, M. D. *J. Chem. Phys.* **2002**, *116*, 7752.
- (45) Gupta, P. K.; Nguyen, D. A.; Sridhar, T. *Phys. Fluids* **2000**, *12*, 1296.
- (46) Rotne, J.; Prager, S. J. *J. Chem. Phys.* **1969**, *50*, 4831.

MA0491255